Scientific Research Publishing

# Preparation of Novel Mesoporous Photocatalyst $Bi_4O_5Br_2$/SBA-15 with Enhanced Visible-Light Catalytic Activity

## Youju Shu[1*], Shengrong Yan[2], Kaijie Dong[2], Jiwei Chen[2]

[1]Graduate School of Life and Environmental Sciences, University of Tsukuba, Tsukuba, Japan
[2]School of Chemical and Material Engineering, Jiangnan University, Wuxi, China
Email: *shuyouju@126.com

## Abstract

Photocatalysis is one of the most promising methods owing to its great potential to relieve environmental issue. To construct efficient photocatalyst with low energy consumption, mild catalytic conditions, and stable chemical properties are highly desired. In this work, a novel, highly active and environmental friendly mesoporous photocatalyst $Bi_4O_5Br_2$/SBA-15 was synthesized by hydrothermal method, and its characteristics and visible-light catalytic activity were investigated. The synthesized photocatalyst consisted of Langmuir type IV hysteresis loops, which was confirmed to be a composite material with mesoporous structure. It exhibited a high visible-light absorption intensity and a low recombination rate of photo-generated electrons and holes. When the mass ratio of $Bi/SiO_2$ was 30/100 during the synthesis, the obtained photocatalyst ($Bi_{30}$/SBA-15) reflected the fastest Rhodamine B (RhB) removal rate and achieved 100% decolorization of RhB by both adsorption and degradation process. This high decolorization efficiency can also be maintained and realized by recycling the used composite in practice. The enhanced visible-light photocatalytic activity of novel $Bi_4O_5Br_2$/SBA-15 photocatalyst can be ascribed to the existing active sites both inside and outside SBA-15 which enhanced the separation of photo-generated electrons and holes.

## Keywords

Mesoporous Materials, $Bi_4O_5Br_2$/SBA-15, Visible-Light Photocatalytic Activity

## 1. Introduction

Photocatalytic technology has been considered as a promising method for

wastewater treatment [1]. Highly efficient photocatalysts with low energy consumption, mild catalytic conditions, and stable chemical properties are most feasible in practice. Recently, bismuth-based photocatalyst has aroused much attention because of the excellent optical properties and visible-light photocatalytic activity [2], such as $Bi_2MoO_6$ [1], $BiWO_4$ [2], $Bi_4Ti_3O_{12}$ [3], BiOX [4] (X = F, Cl, Br, I), $Bi_4O_5Br_2$ [5] and so on. Among them, $Bi_4O_5Br_2$ is a new type of bismuth-based semiconductor photocatalytic material, and possesses good photoelectric properties. The crystal structure of $Bi_4O_5Br_2$ is similar with BiOX, which belongs to the tetragonal crystal form [6]. $Bi_4O_5Br_2$ has a layered structure composed of $[Bi_2O_2]^{2+}$ and $Bi^{3+}$. The layers are respectively distributed with $X^-$ and $O_2^-$, with the lower layer being $Bi^{3+}$ and the next layer being $O_2^-$. $X^-$ with the $O_2^-$ is arranged in a staggered 45 degree. In the layered crystal structure of $Bi_4O_5Br_2$, the halogen ion layer and the $[Bi_2O_2]^{2+}$ ion layer are alternately arranged along the c-axis, with Van der Waals force between the two halogen ion layers allowing the layered structure to dissociate in the easy [001] direction. There is a strong binding force in the $[Bi_2O_2]^{2+}$ layer, and the dissociation of the double halogen ion layer has an electric field, thus the photoelectron-hole separation efficiency of $Bi_4O_5Br_2$ surface can be greatly improved.

Further, $Bi_4O_5Br_2$ can be modified to enhance the separation rate of photogenerated electron and holes by using halogen atoms adjustment [7] [8] [9] and breaking the stoichiometric layered structure to form a nonstoichiometric layered structure [10] [11] [12] [13], such as $Bi_4O_5Br_2$ [10] [11], $Bi_3O_4Br$ [12] and $Bi_{24}O_{31}Br_{10}$ [13]. Compared with other bismuth-based photocatalyst, $Bi_4O_5Br_2$ has some advantages such as special facets, excellent catalytic activity, high separation rate of photo generated electron and holes, environmental friendliness and simple synthesis methods [5] [14].

However, the shortcomings of small specific surface area, poor thermal stability, difficulty in recovery and agglomeration for $Bi_4O_5Br_2$ should be overcome, and immobilization of $Bi_4O_5Br_2$ provided a feasible method. Activated carbon, $ZrO_2$, $SiO_2$ and zeolite molecular sieves had been used as carrier for the immobilization of semiconductors. Among these materials, disordered porous structure and stability limited the application on photocatalyst modification. SBA-15 is a kind of silicon-based molecular sieves with self-ordered mesoporous material, which has uniform pore size, large pore structure, high surface area and good stability in acid and alkaline conditions [15] [16]. However, no report could be found on SBA-15 supported $Bi_4O_5Br_2$ semiconductor composite photocatalysts. Moreover, after$Bi_4O_5Br_2$ loading on SBA-15, the photoelectron migration on the surface of the photocatalyst and the recombination rate of photogenerated electrons and holes have not been studied yet.

In this study, $Bi_4O_5Br_2$/SBA-15 photocatalytic material was synthesized by sol-gel method, *i.e.* $Bi_4O_5Br_2$ was grafted onto the surface of SBA-15. The morphology, specific surface area, loading ratio and optical properties of synthesized $Bi_4O_5Br_2$/SBA-15 were characterized and the visible light catalytic activity was investigated by using Rhodamine B (RhB) as a target contaminant, the different

decolorization capacities of the synthesized photocatalysts (obtained under different loading ratio of $Bi_4O_5Br_2$/SBA-15) were investigated. At the same time, the photocatalysis stability and reusability of the newly synthesized $Bi_4O_5Br_2$/SBA-15 was evaluated.

## 2. Experimental Section

### 2.1. Synthesis of $Bi_4O_5Br_2$/SBA-15 Mesoporous Materials

$Bi_4O_5Br_2$/SBA-15 was prepared through the following two steps. The first step was to synthesize $Bi_4O_5Br_2$ with solvothermal method. Typically, under stirring at 100 rpm, cetyl trimethyl ammonium bromide (CTAB, 1.5 mmol) and $Bi(NO_3)_3 \cdot 5H_2O$ (1.5 mmol) were added and dissolved in the glycerol solution (15 mL glycerol and 6 mL deionized water), and the stirring lasted for 30 min. Then after 0.1 g polyethylene glycol-10,000 (PEG-10,000) being added to the mixture with pH adjusted to 11.0, the obtained mixture was solvothermally treated at 140°C for 24 h. The solid obtained after centrifugation was washed with water and ethanol for 5 times, and then dried at 50°C for 12 h.

In the second step, $Bi_4O_5Br_2$/SBA-15 was prepared by sol-gel method. In a typical run, 2.0 g polyether $P_{123}$ (PEO-PPO-PEO) was mixed with 65 mL deionized water at room temperature under stirring for 3 h. 10 ml HCl (2 mol/L) was then dropped into the above mixture at 40°C under stirring for 1 h. The synthesized $Bi_4O_5Br_2$ in the first step was added into the above mixture at a different mass ratio of $Bi/SiO_2$ of 20/100, 30/100, 40/100, and 50/100. After stirring for 1 hour, 4.5 g tetraethyl orthosilicate (TEOS) was slowly dropped into the mixture at 4°C under stirring for 24 h. The obtained mixture was later solvothermally treated at 140°C for 24 h. The mixture was centrifuged, washed, and dried at 60°C for 8 h. The obtained solid samples were calcined at 550°C in air atmosphere for 6 h, which were labeled as $Bi_{20}$/SBA-15, $Bi_{30}$/SBA-15, $Bi_{40}$/SBA-15, and $Bi_{50}$/SBA-15, respectively.

### 2.2. Characterization

X-ray diffraction (XRD) measurement was conducted on a D/max-2550 PC X-ray diffractometer. Scanning electron microscope (SEM, Hitachi S-4800) and transmission electron microscope (TEM, JEOL JEM-2100 high-resolution transmission electron microscope (HRTEM)) were also used to characterize the obtained photocatalysts. The optical diffuse reflectance spectra (DRS) were acquired with a UV-vis-NIR scanning spectrophotometer. The photoluminescence (PL) spectra were detected by using a spectrophotometer (FS5, England). The Brunauer-Emmett-Teller (BET) surface area was determined by a micromeretics ASAP 2010 apparatus with a multipoint BET method using the adsorption data in the relative pressure $(P/P_0)$ range of 0.05 - 0.3. The desorption isotherm was used to determine the pore size distribution according to the Barrett-Joyner-Halenda (BJH) method. X-ray photoelectron spectra (XPS) analysis was performed on a PHI-5400 instrument with Mg K$\alpha$ as the X-ray source under a pressure of 1.33 ×

$10^{-7}$ Pa and a step of 0.05 eV. The C (1s) level (285.0 eV) was taken as the reference binding energy.

## 2.3. Photocatalytic Activity Measurement

RhB solution (10 mg/L) was used to evaluate the photocatalytic activity of the obtained composites under visible light irradiation. A 300 W xenon lamp with a 420 nm cut-off filter provided visible light irradiation. A same photocatalyst dosage of 0.2 g/L was used for all the tests. Prior to visible light irradiation, the mixtures of RhB and photocatalyst were magnetically stirred in the dark for 30 min to ensure the establishment of an adsorption-desorption equilibrium of RhB on the catalyst surface. Then, the solution was irradiated by xenon lamp. At given irradiation time intervals, 4 mL of the mixtures were collected and centrifuged at 10,000 rpm for 10 min to remove the photocatalysts. The residual concentration of RhB was analyzed with a 725N UV-v is spectrophotometer. The RhB solution temperature was controlled at 19°C ± 2°C during the whole experiment.

## 2.4. Active Species Trapping Experiment

To detect the active species produced during the photocatalytic process, such as superoxide radical ($\cdot O_2^-$), hole ($h^+$) and hydroxyl radical ($\cdot OH$), active species trapping experiments were carried out by adding scavenger into different RhB solutions. The scavengers were p-benzoquinone (p-BQ), sodium oxalate (SO), and iso-propanol (IPA), respectively. The dosage of each scavenger was 1.0 mmol/L.

## 3. Results and Discussion

### 3.1. Characterization of $Bi_4O_5Br_2$/SBA-15 Composites

**Figure 1(a)** showed the small angle XRD pattern of SBA-15 with different loading ratio of $Bi_4O_5Br_2$. It can be seen that all the synthesized samples have a strong diffraction peak ($2\theta = 0.90°$ to $1.0°$) and two weak diffraction peaks ($2\theta = 1.3°$ to $1.8°$) in the range of small angle ($2\theta = 0.3°$ to $5°$). These characteristic peaks are
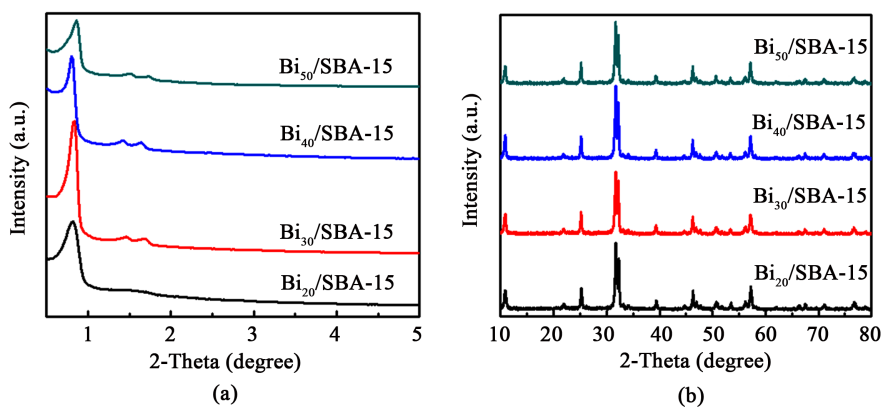


**Figure 1.** Small angle XRD (a) and wide angle XRD (b) of the synthesized materials.

coincident with the crystal plane diffraction peaks of (100), (110), and (200) in the two-dimensional hexagonal structure of SBA-15, respectively. This observation reveals the presence of a typical two-dimensional hexagonal ordered mesoporous structure [17], further indicating that the loading of $Bi_4O_5Br_2$ did not change the mesoporous structure of SBA-15. The diffraction peaks shifted to higher angles from $Bi_{20}$/SBA-15 to $Bi_{50}$/SBA-15, meaning that their pore diameters gradually decreased along with the increase of loading ratio, and $Bi_{20}$/SBA-15 has the largest pore diameter [18]. On the other hand, the diffraction peak intensity was first increased and then decreased, with the intensity of $Bi_{30}$/SBA-15 diffraction peak being the highest. This observation indicated that the mesoporous structure of the synthesized $Bi_{30}$/SBA-15 is the most regular among the synthesized samples, since the high intensity of peaks is attributable to the incorporation of Bi into the mesoporous silica matrix, creating new crystal facets on mesoporous structure [19].

Figure 1(b) showed the wide angle XRD patterns of the synthesized $Bi_4O_5Br_2$/SBA-15 samples. As seen, all the samples had similar characteristic peaks, and the corresponding positions of the characteristic peaks were 11.2˚, 25.0˚, 31.5˚, 39.2˚, 46.2˚, 53.5˚, 57.2˚, 67.1˚, and 76.0˚, respectively. These peaks were corresponding to the tetragonal phase of $Bi_4O_5Br_2$ (standard card JCPDS No. 09-0699), which were consistent with the following crystal planes of $Bi_4O_5Br_2$ (001), (011), (012), (110), (112), (020), (211), (220), and (130), respectively. Especially, the strongest diffraction peak intensity was detected at 31.5˚, indicating that the tetragonal $Bi_4O_5Br_2$ grows along with the (012) crystal plane.

Table 1 summarized the specific surface area, pore volume and average pore size of the composites. The pore diameters of $Bi_{20}$/SBA-15, $Bi_{30}$/SBA-15, $Bi_{40}$/SBA-15, and $Bi_{50}$/SBA-15 firstly increased and then decreased. This variation trend was consistent with the results from the small angle XRD. With the increase of $Bi_4O_5Br_2$ loading ratio, both specific surface area and pore volume of the synthesized photocatalysts showed a decreasing trend, possibly due to the relatively bigger size of $Bi_4O_5Br_2$ particles which are easy to block a part of the pores. This phenomenon implied that the adsorption capacity of $Bi_4O_5Br_2$/SBA-15 might gradually decrease when compared to SBA-15 [20]. Figure 2 illustrated the nitrogen sorption-desorption isotherm curves of the synthesized composites. All the curves exhibited the Langmuir type IV hysteresis loops, suggesting that the synthesized $Bi_{20}$/SBA-15, $Bi_{30}$/SBA-15, $Bi_{40}$/SBA-15, and $Bi_{50}$/SBA-15 have the characteristics of mesoporous materials with ordered mesoporous structures.

**Table 1.** Surface area, pore volume and average pore size of the synthesized materials.

| Samples | Specific area ($m^2$/g) | Pore volume ($cm^3$/g) | Average diameter (nm) |
|---|---|---|---|
| $Bi_{20}$/SBA-15 | 156 | 0.26 | 6.6 |
| $Bi_{30}$/SBA-15 | 84 | 0.16 | 6.5 |
| $Bi_{40}$/SBA-15 | 62 | 0.11 | 6.3 |
| $Bi_{50}$/SBA-15 | 51 | 0.10 | 6.0 |
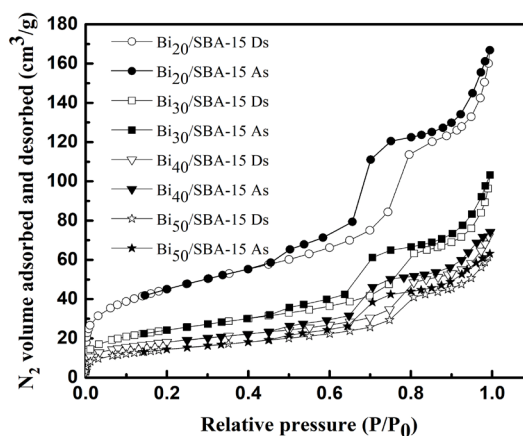
**Figure 2.** Nitrogen adsorption-desorption isotherms of the samples (Notes: Ds and As denotes adsorbed and desorbed).

The SEM and TEM images of SBA-15, $Bi_4O_5Br_2$, and $Bi_4O_5Br_2$/SBA-15 showed in **Figure 3**. The image of pure SBA-15 clearly has well-ordered mesoporous hexagonal arrays (**Figure 3(a)**) and one-dimensional channels of the mesoporous structure (**Figure 3(d)**) with a diameter of 7.3 nm. The results demonstrated the high ordering level obtained from silica synthesis and confirmed the pore size distribution [21]. **Figure 3(b)** and **Figure 3(e)** showed the morphology of $Bi_4O_5Br_2$ with special nanosheets. No diffraction spots or diffraction rings were observed in **Figure 3(d)**, revealing the non-crystallinity silica characteristics of SBA-15. **Figure 3(c)** and **Figure 3(f)** show the images of $Bi_{30}$/SBA-15 sample. Smaller particles were found to spread over larger particles in all the images, and the larger particles were identified as SBA-15 silica because of their characteristic lines of mesoporous material channels. The smaller particles spread on the SBA-15 reflected the same texture as the larger particles, indicating that they belong to the same type of materials. These agglomerations of nanoparticles were mainly in the range of 100 nm. This observation is consistent with the $Bi_4O_5Br_2$ phase from the XRD patterns. However, as it can be seen from **Figure 3(c)** and **Figure 3(f)**, $Bi_4O_5Br_2$ as rods or spheres were distributed on the surface of the SBA-15. **Figure 3(c)** and **Figure 3(f)** also showed that $Bi_4O_5Br_2$ might be chemically bonded to the surface of SBA-15, not simply loaded on the surface, which may produce stable photocatalytic components thus exhibit photocatalytic activity, thereby increase the possibility of recirculation of the photocatalytic material.

In order to study the elemental composition and valence state of the photocatalytic materials, XPS analysis of $Bi_{30}$/SBA-15 was performed (**Figure 4**). The survey XPS spectrum of $Bi_{30}$/SBA-15 confirmed the existents of Si, C, O, Bi, and Br elements. The appearance of element C may be caused by $CO_2$ from the sample absorption of air during the analysis [22]. In **Figure 4(b)**, the peak at 103.6 eV is corresponding to Si 2p spectrum, which is the characteristic peak of Si-O-Si band in $SiO_2$ of SBA-15 and the characteristic peak of $Si^{4+}$ [23] [24] [25]. A high resolution energy spectrum of O 1s with two main peaks (**Figure 4(c)**),
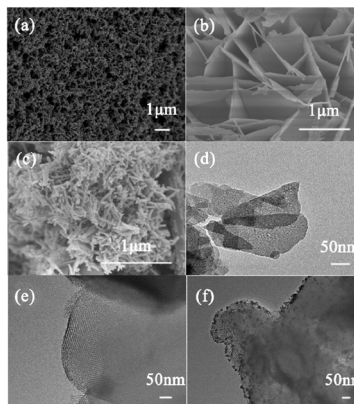
**Figure 3.** SEM images of SBA-15 (a); $Bi_4O_5Br_2$ (b) and $Bi_4O_5Br_2$/SBA-15 (c); and TEM images of SBA-15 (d); $Bi_4O_5Br_2$ (e) and $Bi_4O_5Br_2$/SBA-15 (f).
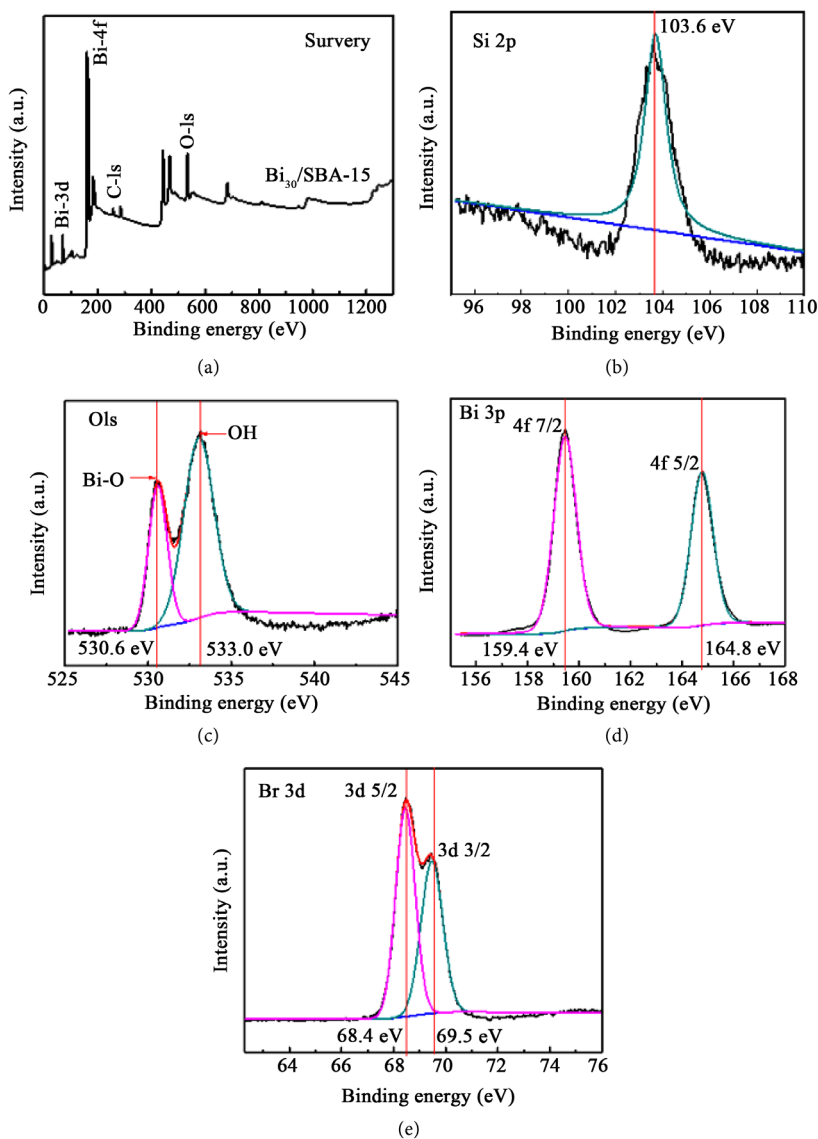


**Figure 4.** XPS spectra of $Bi_{30}$/SBA-15: full spectrum (a); Si 2p (b); O 1s (c); Bi 4f (d); and Br 3d (e).

530.6 and 533.0 eV, respectively, was obtained. The main peak 530.6 eV is assigned to the lattice oxygen of Bi-O bond in $[Bi_2O_2]^{2+}$ in the layered $Bi_4O_5Br_2$/SBA-15, while the peak at 533.0 eV is chemisorbed oxygen and $OH^-$ adsorbed on the surface of the material [26]. The Bi 4f spectrum displayed in **Figure 4(d)** contains two peaks at binding energy of 159.4 and 164.8 eV, which is attributed to Bi 4f7/2 and 4f5/2 [27] [28]. **Figure 4(e)** showed that the high-resolution energy spectrum belongs to Br 3d. As its two partial peaks are 68.4 and 69.5 eV [29] [30] [31] [32], respectively, and its corresponding spectra were 3d5/2 and 3d3/2, thus its valence was −1. Results of the XPS spectra indicated that the measured elements corresponded to the elements in the synthesized samples.

**Figure 5** showed the UV-vis DRS of $Bi_4O_5Br_2$/SBA-15 at different loading ratio of the two major materials. As seen, all the samples had a certain absorption under UV light and the absorption efficiency of $Bi_{20}$/SBA-15 was the highest. As shown in **Figure 5(a)**, all the composite samples exhibited significant absorption sidebands in the visible light range around 410, 415, 430, and 435 nm, respectively. In addition, with the increase of the loading ratio, the absorption wavelength of visible light by the photocatalytic material was red-shifted, and the light response range was expanded. Among them, the bandgap of $Bi_{50}$/SBA-15 was determined to be the narrowest, resulting in the highest utilization rate of visible light. This could be further analyzed by using the Kubelka-Munk formula [33]:

$$\alpha h v = A \left( h v - E_g \right)^{n/2}$$

where $\alpha$ is the light absorption index, namely Abs, $h$ is the Prandtl constant, $v$ is the frequency, $A$ is the constant, $E_g$ is the semiconductor band gap energy. Since $Bi_4O_5Br_2$ is an indirect bandgap semiconductor, $n = 2$. $E_g = h v = 1240/\lambda$, the unit is electron volts (eV), $E_g$ is the abscissa, $(\alpha h v)^{1/n}$ was plotted on the ordinate, and band gap energy spectra of different samples were obtained (**Figure 5(b)**). It can be seen from **Figure 5(b)** that the bandgap energy of the samples decreased from about 3.30 eV to 3.10 eV with the increase of $Bi_4O_5Br_2$ loading ratio, and this may be caused by the agglomeration of nanoparticles [34].



(a)                    (b)
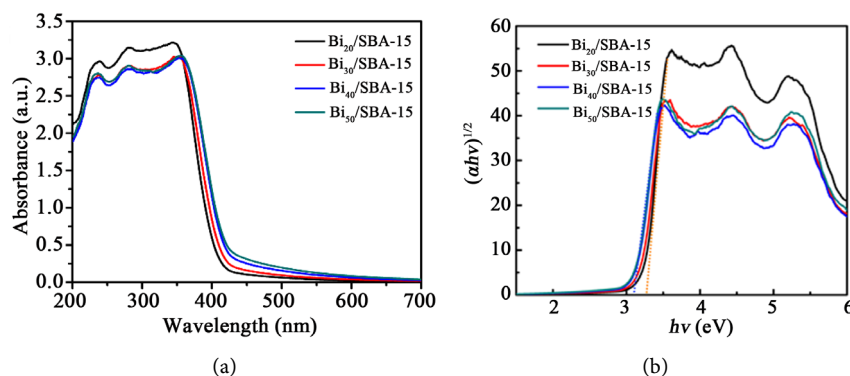
**Figure 5.** UV-vis absorption spectrogram (a) and $(\alpha h v)^{1/2}$-($h v$) curves (b) for different synthesized materials.

539

## 3.2. Evaluation on Photocatalytic Performance

**Figure 6(a)** demonstrated the photodegradation curves and degradation curves for $Bi_{20}$/SBA-15, $Bi_{30}$/SBA-15, $Bi_{40}$/SBA-15, and $Bi_{50}$/SBA-15 at 25˚C, respectively. The abscissa was the reaction time for dark adsorption and photodegradation, and the ordinate was the concentration of RhB remained. From **Figure 6(a)**, it can be seen that the $Bi_4O_5Br_2$ at different loading ratio possessed strong absorption capacity for RhB, which could remove RhB from 30% to 65% within 1 h of adsorption in dark, following a descending order of $Bi_{30}$/SBA-15 > $Bi_{20}$/SBA-15 > $Bi_{40}$/SBA-15 > $Bi_{50}$/SBA-15. The residual RhB in solution was removed by photodegradation under visible light. During the whole reaction process, the removal of RhB with $Bi_{30}$/SBA-15 was the fastest. Although the band gaps of $Bi_{50}$/SBA-15 and $Bi_{40}$/SBA-15 were narrower than that of $Bi_{30}$/SBA-15, the RhB removal rates for $Bi_{50}$/SBA-15 and $Bi_{40}$/SBA-15 were lower than that for $Bi_{30}$/SBA-15. It might be the structure of SBA-15 was destroyed with big size nanoparticles which blocked the porous for adsorption of RhB onto the surface of SBA-15.

**Figure 6(b)** showed the fluorescence spectra of synthesized materials at different loading ratio of $Bi_4O_5Br_2$. The test was conducted at room temperature with the excitation wavelength of 250 nm. It can be seen that the peak shapes and positions of the four samples are similar, with the largest peak around 432 nm and another two weak peaks, indicating that the $Bi_4O_5Br_2$/SBA-15 was excited at 432 nm by the sunlight with the occurrence of electronic transitions and generation of photogenerated electron-hole pairs. Photoluminescence spectroscopy is an important approach to characterize the photoelectron-hole recombination rate of photocatalysts. The recombination rate of photoelectron-holes is proportional to the light intensity. Therefore, the photogenerated electron-holes of photocatalysts can be compared by using the light intensities. The light intensity of $Bi_{50}$/SBA-15 was the largest, followed by $Bi_{40}$/SBA-15, $Bi_{30}$/SBA-15, and $Bi_{20}$/SBA-15. The separation effect of $Bi_{30}$/SBA-15 was relatively high, which might be the major reason for its better photocatalytic effect than others. The
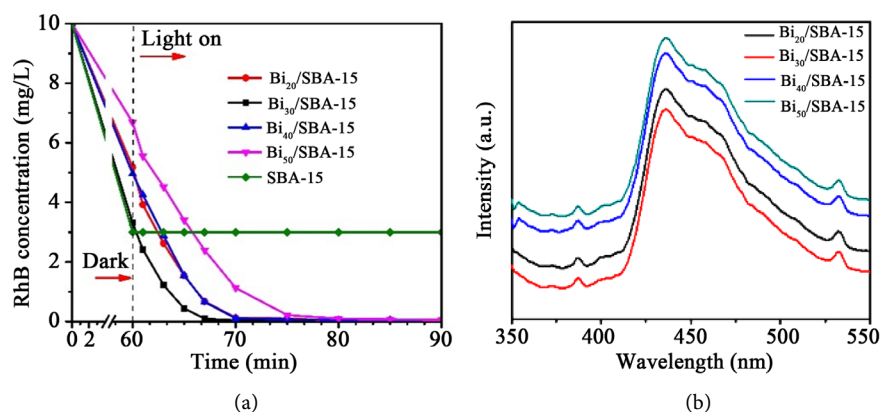


**Figure 6.** Photocatalytic performance (a) and photoluminescence spectra (b) of the tested samples.

reason was the active site was present inside and outside the SBA-15 first increasing with $Bi_4O_5Br_2$ loading increase, which indicated the separation rate of electron and hole was enhanced, and then decreased which explored that the active site decrease with excess loading of nanoparticles of $Bi_4O_5Br_2$ blocked the porous.

### 3.3. Active Species and Stability Analysis

$Bi_4O_5Br_2$ is a lamellar structure composed of a $[Bi_2O_2]^{2+}$ layer and a double Br-layer interlaced, with an internal electrostatic field established between the layers. When a semiconductor was excited under visible light irradiation, photocurrent could be formed if the photoelectrons move in a fixed direction. A stronger photocurrent indicated more effective separation of electron-holes and higher photocatalytic performance of the semiconductor as well. In the photocatalytic decolorization of RhB, the capture agents SO, IPA and p-BQ were individually added to capture the active species $h^+$, •OH and •$O_2^-$ (**Figure 7(a)**). As shown in **Figure 7(a)**, the photocatalytic activity of $Bi_{30}$/SBA-15 slightly decreased when the capture agent IPA was added. In the case of capture agent p-BQ, the photocatalytic activity of the synthesized photocatalyst was significantly reduced after its addition in the photocatalytic process. When adding SO, the photocatalyst showed almost no effect on the decolorization of RhB, implying the catalytic activity was significantly inhibited. The result indicated that h+ played the main role in RhB degradation under visible light.

For evaluation on the stability of the photocatalytic activity of the prepared $Bi_4O_5Br_2$/SBA-15, sample $Bi_{30}$/SBA-15 was selected to remove RhB for 5 times (**Figure 7(b)**). Results showed that after 5 cycles of reutilization of $Bi_{30}$/SBA-15, its photocatalytic activity remained almost unchanged, and about 99.42% RhB was removed.

### 4. Conclusion

A sol-gel thermal method was used to synthesize the Bi4O5Br2/SBA-15 photocatalytic materials. $Bi_4O_5Br_2$ loading on the SBA-15 had some positive effects on
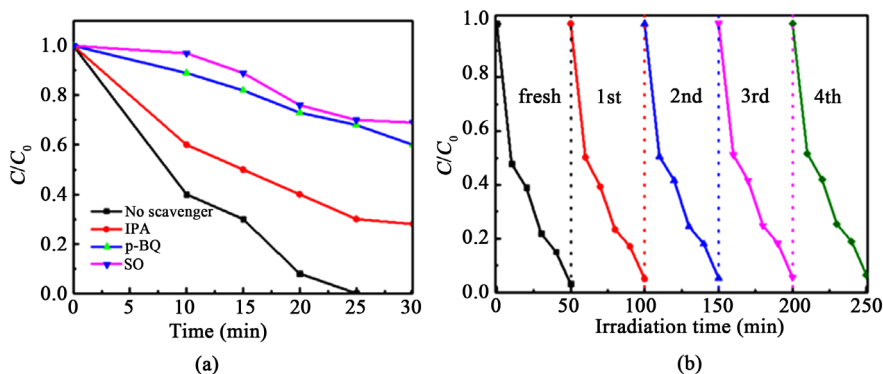


**Figure 7.** Effects of various scavengers (SO, IPA and p-BQ) on RhB removal with $Bi_{30}$/SBA-15 (a) and cycle runs of $Bi_{30}$/SBA-15 for RhB decolorization (b).

RhB degradation. The photocatalytic activity of $Bi_4O_5Br_2$/SBA-15 firstly increased and then decreased with the increase of $Bi_4O_5Br_2$ loading. The highest RhB removal rate was obtained by using $Bi_{30}$/SBA-15. The reusability of the catalyst $Bi_{30}$/SBA-15 was investigated. This work provided a new thought for designing the photocatalyst with high efficiency and stability for environmental remediation.

## Conflicts of Interest

The authors declare no conflicts of interest regarding the publication of this paper.

## References

[1] Di, J., Xia, J., Ji, M., Li, H., Xu, H., Li, H. and Chen, R. (2015) The Synergistic Role of Carbon Quantum Dots for the Improved Photocatalytic Performance of $Bi_2MoO_6$. *Nanoscale*, **7**, 11433-11443. https://doi.org/10.1039/C5NR01350J

[2] Li, C., Chen, G., Sun, J., Zhao, J. and Han, Z. (2015) A Novel Mesoporous Single-Crystal-Like $Bi_2WO_6$ with Enhanced Photocatalytic Activity for Pollutants Degradation and Oxygen Production. *ACS Applied Materials & Interfaces*, **7**, 25716-25724. https://doi.org/10.1021/acsami.5b06995

[3] Hou, D., Luo, W., Huang, Y., Yu, J. and Hu, X. (2013) Synthesis of Porous $Bi_4Ti_3O_{12}$ Nanofibers by Electrospinning and Their Enhanced Visible-Light-Driven Photocatalytic Properties. *Nanoscale*, **592**, 2028-2035. https://doi.org/10.1039/c2nr33750a

[4] Zhao, J., Lv, X., Wang, X., Yang, J., Yang, X. and Lu, X. (2015) Fabrication of BiOX (X=Cl, Br, and I) Nanosheeted Films by Anodization and their Photocatalytic Properties. *Materials Letters*, **158**, 40-44.
https://doi.org/10.1016/j.matlet.2015.05.037

[5] Di, J., Xia, J., Ji, M., Yin, S., Li, H., Xu, H., Zhang, Q. and Li, H. (2015) Controllable Synthesis of $Bi_4O_5Br_2$ Ultrathin Nanosheets for Photocatalytic Removal of Ciprofloxacin and Mechanism Insight. *Journal of Materials Chemistry A*, **3**, 15108-15118.
https://doi.org/10.1039/C5TA02388B

[6] Song, J., Mao, C., Niu, H., Shen, Y. and Zhang, S. (2010) Hierarchical Structured Bismuth Oxychlorides: Self-Assembly from Nanoplates to Nanoflowers via a Solvothermal Route and Their Photocatalytic Properties. *Crystengcomm*, **12**, 3875-3881.
https://doi.org/10.1039/c003497p

[7] Zhang, X, Wang, L., Wang, C., Wang, W., Chen, Y., Huang, Y., Li, W., Feng, Y. and Yu, H. (2015) Synthesis of $BiOCl_xBr_{1-x}$ Nanoplate Solid Solutions as a Robust Photocatalyst with Tunable Band Structure. *Chemistry—A European Journal*, **21**, 11872-11877. https://doi.org/10.1002/chem.201501427

[8] Yang, Z., Cheng F., Dong X. and Cui F. (2015) Controllable *in Situ* Synthesis of $BiOBr_xI_{1-x}$ Solid Solution on Reduced Graphene Oxide with Enhanced Visible Light Photocatalytic Performance. *RSC Advances*, **5**, 68151-68158.
https://doi.org/10.1039/C5RA08416D

[9] Kim, W., Pradhan, D., Min, B. and Sohn, Y. (2014) Adsorption/Photocatalytic Activity and Fundamental Natures of BiOCl and $BiOCl_xI_{1-x}$ Prepared in Water and Ethylene Glycol Environments, and Ag and Au-Doping Effects. *Applied Catalysis B: Environmental*, **147**, 711-725. https://doi.org/10.1016/j.apcatb.2013.10.008

[10] Bai, Y., Chen, T., Wang, P., Wang, L. and Ye, L. (2016) Bismuth-Rich $Bi_4O_5X_2$ (X =

Br, and I) Nanosheets with Dominant {101} Facets Exposure for Photocatalytic H$_2$ Evolution. *Chemical Engineering Journal*, **304**, 454-460. https://doi.org/10.1016/j.cej.2016.06.100

[11]  Ding, S., Mao, D., Yang, S., Wang, F., Meng, L., Han, M., He, H., Sun, C. and Xu, B. (2017) Graphene-Analogue h-BN Coupled Bi-Rich Bi$_4$O$_5$Br$_2$ Layered Microspheres for Enhanced Visible-Light Photocatalytic Activity and Mechanism Insight. *Applied Catalysis B: Environmental*, **3**, 386-399. https://doi.org/10.1016/j.apcatb.2017.04.002

[12]  Wang, J., Yu, Y., Zhang, L., Wang, J., Yu, Y. and Zhang, L. (2013) Highly Efficient Photocatalytic Removal of Sodium Pentachlorophenate with Bi$_3$O$_4$Br under Visible Light. *Applied Catalyst B-Environmental*, **136-137**, 112-121. https://doi.org/10.1016/j.apcatb.2013.02.009

[13]  Song, J., Zhang, L., Yang, J., Huang, X. and Hu, J. (2017) Hierarchical Porous Bi$_{24}$O$_{31}$Br$_{10}$ Microarchitectures Assembled by Ultrathin Nanosheets with Strong Adsorption and Excellent Photocatalytic Performances. *Materials & Design*, **5**, 128-136. https://doi.org/10.1016/j.matdes.2017.03.046

[14]  Xiao, X., Lu, M., Nan, J., Zuo, X., Zhang, W., Liu, S. and Wang, S. (2017) Rapid Microwave Synthesis of I-Doped Bi$_4$O$_5$Br$_2$ with Significantly Enhanced Visible-Light Photocatalysis for Degradation of Multiple Parabens. *Applied Catalysis B: Environmental*, **218**, 398-408. https://doi.org/10.1016/j.apcatb.2017.06.074

[15]  Yuan, E., Wu, C., Liu, G., Li, G. and Wang, L. (2018) Effects of SBA-15 Physicochemical Properties on Performance of Pd/SBA-15 Catalysts in 2-Ethyl-Anthraquinone Hydrogenation. *Journal of Industrial and Engineering Chemistry*, **66**, 158-167. https://doi.org/10.1016/j.jiec.2018.05.025

[16]  Li, G., Wang, B., Xu, W., Han, Y. and Sun, Q. (2018) Rapid TiO$_2$/SBA-15 Synthesis from Ilmenite and Use in Photocatalytic Degradation of Dimethoate under Simulated Solar Light. *Dyes and Pigments*, **155**, 265-267. https://doi.org/10.1016/j.dyepig.2018.03.058

[17]  Liu, J., Huang, H., Liu, X., Xiao, J., Zhong, S., She, X., Fu, Z., Kirk, S.R. and Yin, D. (2017) Preparation of Fe$_2$O$_3$ Doped SBA-15 for Vapor Phase Ortho-Position C-Alkylation of Phenol with Methanol. *Catalysis Communications*, **92**, 90-94. https://doi.org/10.1016/j.catcom.2017.01.015

[18]  Zhang, Z., Luo, Y., Guo, Y., Shi, W., Wang, W., Zhang, B., Zhang, R., Bao, X., Wu, S. and Cui, F. (2018) Pd and Pt Nanoparticles Supported on the Mesoporous Silica Molecular Sieve SBA-15 with Enhanced Activity and Stability in Catalytic Bromate Reduction. *Chemical Engineering Journal*, **344**, 114-123. https://doi.org/10.1016/j.cej.2018.03.056

[19]  Chen, D. and Ray, A. (1998) Photodegradation Kinetics of 4-Nitrophenol in TiO$_2$ Suspension. *Water Research*, **32**, 3223-3234. https://doi.org/10.1016/S0043-1354(98)00118-3

[20]  Cheng, M., Zhao, H., Yang, J., Zhao, J., Yan, L., Song, H. and Chou, L. (2018) The Catalytic Dehydrogenation of Isobutane and the Stability Enhancement over Fe Incorporated SBA-15. *Microporous Mesoporous Materials*, **266**, 117-125. https://doi.org/10.1016/j.micromeso.2018.02.046

[21]  Zhao, D., Sun, J., Li, Q. and Stucky, G.D. (2000) Morphological Control of Highly Ordered Mesoporous Silica SBA-15. *Chemical Materials*, **12**, 275-279. https://doi.org/10.1021/cm9911363

[22]  Zhang, M., Shao, C., Mu, J., Huang, X. and Zhang, Z. (2011) Hierarchical Heterostructures of Bi$_2$MoO$_6$ on Carbon Nanofibers: Controllable Solvothermal Fabrication and Enhanced Visible Photocatalytic Properties. *Journal of Materials Chemi-*

*stry*, **22**, 577-584. https://doi.org/10.1039/C1JM13470A

[23] Acosta-Silva, Y.J., Nava, R., Hernández-Morales, V., Macías-Sánchez, S.A., Gómez Herrera, M.L. and Pawelec, B. (2011) Methylene Blue Photodegradation over Titania-Decorated SBA-15. *Aplied Catalyst B: Environmental*, **110**, 108-117.

[24] Liu, C., Lin, X., Li, Y., Xu, P., Li, M. and Chen, F. (2016) Enhanced Photocatalytic Performance of Mesoporous $TiO_2$ Coated SBA-15 Nanocomposites Fabricated through Anovel Approach: Supercritical Deposition Aided by Liquid-Crystal Template. *Material Research Bulletin*, **75**, 25-34.
https://doi.org/10.1016/j.materresbull.2015.10.052

[25] Xia, F., Ou, E., Wang, L. and Wang, J. (2008) Photocatalytic Degradation of Dyes over Cobalt Doped Mesoporous SBA-15 under Sunlight. *Dyes Pigment*, **76**, 76-81.
https://doi.org/10.1016/j.dyepig.2006.08.008

[26] Wang, Y., Bai, X., Pan, C., He, J. and Zhu, Y. (2012) Enhancement of Photocatalytic Activity of $Bi_2WO_6$ Hybridized with Graphite-Like $C_3N_4$. *Journal of Materials Chemistry*, **22**, 11568-11573. https://doi.org/10.1039/c2jm16873a

[27] Zhou, L., Wang, W., Liu, S., Zhang, L., Xu, H. and Zhu, W. (2006) A Sonochemical Route to Visible-Light-Driven High-Activity $BiVO_4$ Photocatalyst. *Journal of Molecular Catalysis A: Chemical*, **252**, 120-124.
https://doi.org/10.1016/j.molcata.2006.01.052

[28] Long, M., Cai, W., Cai, J., Zhou, B., Chai, X. and Wu, Y. (2006) Efficient Photocatalytic Degradation of Phenol over $Co_3O_4$/$BiVO_4$ Composite under Visible Light Irradiation. *The Journal of Physical Chemistry B*, **110**, 20211-20216.
https://doi.org/10.1021/jp063441z

[29] Huo, Y., Zhang, J., Miao, M. and Jin, Y. (2012) Solvothermal Synthesis of Flower-Like BiOBr Microsphere with Highly Visible Light Photocatalytic Performance. *Applied Catalyst B: Environmental*, **111-112**, 334-341.

[30] Feng, Y., Li, L., Li, J., Wang, J. and Liu, L. (2011) Synthesis of Mesoporous BiOBr 3D Microsphere and Their Photodecomposition for Toluene. *Journal Hazard Materials*, **192**, 538-544. https://doi.org/10.1016/j.jhazmat.2011.05.048

[31] Cheng, H., Huang, B., Wang, P., Wang, Z., Lou, Z., Wang, J., Qin, X., Zhang, X. and Dai, Y. (2011) *In Situ* Ion Exchange Synthesis of the Novel Ag/AgBr/BiOBr Hybrid with Highly Efficient Decontamination of Pollutants. *Chemical Communication*, **47**, 7054-7056. https://doi.org/10.1039/c1cc11525a

[32] Li, Y., Wang, Z., Huang, B., Dai, Y., Zhang, X. and Qin, X. (2015) Synthesis of BiOBr-PVP Hybrids with Enhanced Adsorption-Photocatalytic Properties. *Applied Surface Science*, **347**, 258-264. https://doi.org/10.1016/j.apsusc.2015.04.105

[33] Gate, L.F. (1974) Comparison of the Photon Diffusion Model and Kubelka-Munk Equation with the Exact Solution of the Radiative Transport Equation. *Applied Optics*, **13**, 236-238. https://doi.org/10.1364/AO.13.000236

[34] Liu, G., Niu, P., Sun, C., Smith, S., Chen, Z., Lu, G. and Cheng, H. (2010) Unique Electronic Structure Induced High Photoreactivity of Sulfur-Doped Graphitic $C_3N_4$. *Journal American Chemistry Society*, **132**, 11642-11648.
https://doi.org/10.1021/ja103798k